# Revealing the Conversion Mechanism of Transition Metal Oxide Electrodes during Lithiation from First-Principles

Zhenpeng Yao,[†] Soo Kim,[†] Muratahan Aykol,[†,§] Qianqian Li,[†] Jinsong Wu,[†] Jiangang He,[†] and Chris Wolverton*,[†]

[†]Department of Materials Science and Engineering, Northwestern University, 2220 Campus Drive, Evanston, Illinois 60208, United States

ABSTRACT: Transition metal oxides such as Co_3O_4 and NiO are of significant interest as conversion anode materials for lithium-ion batteries (LIBs), due to their remarkably high theoretical capacities and low cost. While many previous experiments have found that the charge/discharge reactions of Co_3O_4 and NiO can be highly reversible, detailed information about the mechanisms of these reactions, such as the origin of the voltage hysteresis (>1.0 V) between the charge/discharge cycles, is still poorly understood. In this work, we develop and utilize a new computational mechanistic approach that helps elucidate the hysteresis and nonequilibrium reaction pathways associated with these conversion materials. We apply this methodology to investigate a variety of lithiation reaction pathways of Co_3O_4 and NiO by systematically exploring the energetics of a large number of equilibrium and nonequilibrium $Li_xCo_3O_4$ ($0 \leq x \leq 8$) and Li_xNiO ($0 \leq x \leq 2$) structural configurations using first-principles calculations. The overall value of the voltages from our nonequilibrium pathway is in much better agreement with experimental lithiation than the calculated equilibrium voltage while the overall value of the latter reasonably agrees with experimental delithiation. Hence, we propose the charge and discharge processes proceed through equilibrium and nonequilibrium reaction paths, respectively, which contribute significantly to the experimentally observed voltage hysteresis in Co_3O_4 and NiO. Additionally, we find a low-energy, lithiated intermediate phase ($Li_3Co_3O_4$) with an oxygen framework equal to that of the initial Co_3O_4 spinel phase. This intermediate phase represents the capacity threshold below which limited volume expansion and better reversibility can be realized and above which reactions lead to structural degradation and huge expansion.
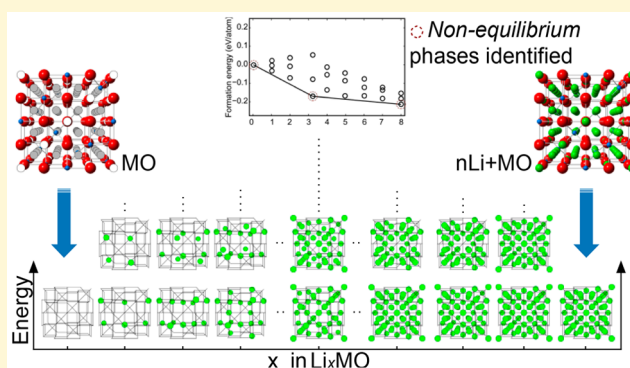
1. INTRODUCTION

Lithium-ion batteries (LIBs) are one of the most prominent electrochemical energy storage technologies, and can be used as the power source in wide-ranging applications such as portable electronic devices, and electric vehicles.[1] There are three major classes of electrode materials in Li-ion batteries: (i) intercalation-type electrodes that preserve the crystal structure framework upon lithiation/delithiation (e.g., $LiCoO_2$, $LiNiO_2$, and $LiFePO_4$),[2,3] (ii) alloying electrodes (e.g., Li/Si, Sn, *etc.*),[4,5] and (iii) conversion-type electrode materials (e.g., Co_3O_4, CoO, and NiO),[6,7] where lithium ions (de)insert via a series of chemical reactions, converting the original compound to a new chemical phase. While intercalation-type electrode materials have their advantages in terms of structural stability and the associated fast and reversible Li$^+$ diffusion within the host structure, the constraint of preserving the crystal structure limits the capacity to the number of available vacant sites that can accommodate Li ions. In contrast, conversion-type materials can achieve a significantly larger capacity by overcoming this inherent structural limitation of intercalation electrodes; however, they pose other problems such as limited

reversibility and voltage hysteresis. In these conversion-type reactions, nonequilibrium phases often form during repeated charging/discharging cycles, and these nonequilibrium pathways directly affect the electrochemical performance.[8-10] A phase transformation of these nonequilibrium phases to their thermodynamically ground-state structures can occur spontaneously (as $t \rightarrow \infty$); however, there may not be sufficient time to allow transformations from nonequilibrium phases into their equilibrium counterparts. The battery performance can be greatly influenced by these nonequilibrium (de)lithiation reactions, that could affect its capacity and cyclability, as well as cause a voltage hysteresis.[11-19] Also, because of the transient nature of these nonequilibrium phases, it can be challenging to identify and characterize them experimentally during electrochemical reactions.[11,13]

Many transition metal oxides (MOs) have been investigated in the past as conversion electrodes,[20,21] exhibiting different

chemical reactions, electrochemical performance, and reversibility. In this work, we investigate Co_3O_4 and NiO conversion-type electrode materials that can achieve a very high reversible capacity of >700 mA h/g.[6] Co_3O_4 and NiO are observed to lithiate at ~1.1 and 0.7 V (vs Li/Li^+), respectively, with a large voltage hysteresis of >1.0 V during charge/discharge runs.[6] While exceptional reversible reactivities of Co_3O_4 and NiO have been achieved in previous experiments,[6,7,22−26] the underlying mechanism during the electrochemical process, and the source of the large hysteresis, has not been fully understood. During the lithiation of Co_3O_4, it was observed that tetrahedral Co cations are displaced into neighboring empty octahedral sites while incoming Li ions occupy the remaining octahedral sites, producing an intermediate, rocksalt-based, nonequilibrium phase with a partial disordered (Li/Co) structure (i.e., $LiCo_3O_4$).[22,27] Further lithiation of $LiCo_3O_4$ leads to a slow extrusion of cobalt at the octahedral sites.[22] The structural evolution beyond that point ($2 < x < 8$, $Li_xCo_3O_4$) is still unclear. The lithiation of NiO is initiated by a quick saturation of near-surface electroactive sites, followed by propagation of these lithiated phases ($Li_2O\cdot Ni$) into the bulk with a "fingerlike" morphology.[28] The conversion-reaction decomposition of Co_3O_4 and NiO in the first cycle involves the formation of amorphous/nanosized metal (e.g., Co and Ni, respectively) and lithia (Li_2O); no crystalline Co, Co_3O_4, Ni, NiO, or Li_2O were identified in fully lithiated samples. In subsequent cycles, the amorphous/nanosized phases of the electrode are preserved.[29] It has been suggested that repeated decomposition and the formation of lithia are facilitated by the nanoscale dimensions and the catalytic activity of the transition metal particles.[25,30,31]

The large voltage hysteresis (>1.0 V) between charge and discharge voltage profiles causes low cycling efficiency of conversion material electrodes and hinders their practical applications. Many efforts have been made to obtain a comprehensive understanding of the origins of the voltage hysteresis. Several hypotheses were suggested based on experimental and computational studies besides the well-known ohmic drop (typically on the magnitude of 0.1 V).[10] We summarize these hypotheses here: (1) *Nano effect*. Nanosized phases, as mentioned above, have been forming repeatedly during the electrochemical lithiation and delithiation of transition metal oxides. The cohesive energy of nanoparticles can be significantly lower than that of the bulk counterpart which can thereby affect the reaction voltages.[32] Doe et al.[14] reported a voltage drop around 0.4 V upon lithiation, assessed using a 1 nm spherical particle of bcc iron. However, we note that the overall effect on the voltage hysteresis of a complete cycle should be more limited since the nanosized phases are formed on both lithiation and delithiation, and the voltage variations due to nanostructuring would presumably affect the charge/discharge voltage in the same direction. (2) *Distinct surface chemistries upon charge and discharge*. Khatib et al.[8] and Meggiolaro et al.[9] demonstrated that the surface reactions are different between the lithiation and delithiation of CoP and MgH_2. The corresponding reaction energy difference contributes to the voltage hysteresis observed during the cycling of CoP (0.41 V) and MgH_2 (0.16 V). However, in the conversion electrodes of the present study the magnitude of voltage hysteresis is much larger, and it is unclear whether the surface reaction mechanism can account for such a large hysteresis. (3) *Compositional inhomogeneity caused by kinetic limitation*. Li et al.[10] and Wang et al.[33] proposed that the distribution of phases

formed upon charge and discharge of FeF_3 could be different because of differences in diffusivity between Fe and F. As a result, a Li-deficient surface forms on charge while a Li-rich surface forms on discharge, setting the system at different potentials versus Li^+/Li^0 and inducing a voltage gap. Therefore, the voltage hysteresis according to this mechanism should be largely alleviated when the particle size is sufficiently reduced, allowing for fast reaction kinetics. For transition metal oxides, however, the hysteresis is generally maintained regardless of particle morphologies, shapes, and sizes of the electrode materials.[34−39] (4) *Different reaction paths upon charge and discharge*. The substantial thermodynamic and kinetic disparities between charge/discharge reaction paths has the possibility to account for the large voltage hysteresis (>1.0 V) observed in conversion oxides like Co_3O_4 and NiO. These disparate pathways have been found in other systems. Yu et al.[40] identified an intermediate phase during the conversion from $LiTiS_2$ to $Cu_{0.5}TiS_2$ while the reconversion reaction exhibits simple two-phase features without any intermediate phase. Similarly, Chang et al.[18] found reaction path differences between the charge and discharge of Cu_2Sb. Boesenberg et al.[41] reported asymmetric pathways during cycling of NiO with the formation of a metastable intermediate phase on delithiation. The reaction path difference was then confirmed by Ponrouch et al.[42]

In recent years, density functional theory (DFT) calculations have been widely used as efficient tools to predict new electrode materials, as well as to improve the existing materials by accurately revealing detailed underlying mechanisms that are often difficult to obtain solely via experiments.[1,43−57] The conversion reaction of Li-MOs at room temperature involves a series of nonequilibrium phases that may be different from their thermodynamic equilibrium counterparts because of other kinetic constraints. Here, we develop a DFT-based methodology to determine the nonequilibrium and equilibrium phase evolution during the lithiation and delithiation processes of MOs, namely, Co_3O_4, and NiO. We predict the corresponding lithiation and delithiation voltage profiles which show similar trends with the experimentally observed discharge and charge voltage curves. We propose that the large voltage hysteresis occurring in Co_3O_4 and NiO can predominantly be attributed to the dramatic difference in reaction pathways between a thermodynamically nonequilibrium lithiation and an equilibrium delithiation. These conversion-type electrodes, when used within the practical capacity thresholds, are predicted to have improved cycling stability and lower voltage hysteresis.

2. METHODOLOGY

2.1. Density Functional Theory Calculations. All DFT calculations were carried out in the Vienna Ab-initio Simulation Package (VASP)[58−61] with the projector augmented wave (PAW) potentials.[62] The generalized gradient approximation (GGA) of Perdew−Becke−Ernzerhof (PBE)[63] was used for the exchange-correlation functional; also, all calculations are spin-polarized. We used a cutoff energy of 520 eV for the plane−wave basis set and Γ-centered k-meshes with the density of 8000 k-points per reciprocal atom in all calculations. We used the DFT + U method with onsite U parameters to treat the 3d electrons of Co and Ni ions. The U values of 3.3 and 6.4 eV were adopted for Co and Ni ions, similar to previous studies by fitting the experimental and calculated formation enthalpy.[64−71] Ferromagnetic (FM) and antiferromagnetic (AFM) spin-polarized configurations were used for Co_3O_4 and NiO,
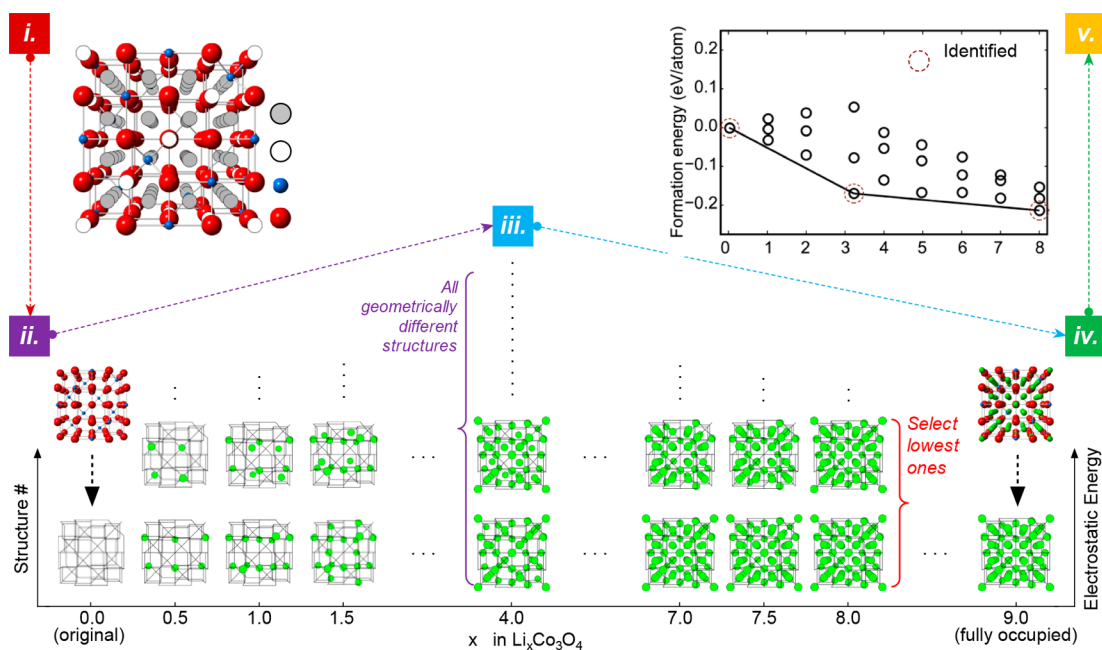
Figure 1. Searching for the nonequilibrium phases through the Li-TMO reactions: an example of Li−Co$_3$O$_4$. The searching process proceeds as follows: (i) Possible insertion sites (T$_d$ and O$_h$) were identified from the original Co$_3$O$_4$ spinel structure. (ii) All symmetrically distinct configurations of Li on the unoccupied sites were generated for each composition using Enum (Li/vacancy orderings are shown by the green circles with the Co$_3$O$_4$ structure visualized by lines).[87−89] (iii) Total energies of all the configurations generated were sampled using electrostatic calculations. (iv) For each composition, corresponding structures were ranked by the total energies, and the three lowest energy structures were further relaxed using DFT. The formation energies for these selected structures were then evaluated. (v) Using formation energies obtained, the nonequilibrium Li−Co$_3$O$_4$ convex hull is built. The composition points located on the convex hull then correspond to the identified nonequilibrium phases.

respectively, since NiO is known to display the antiferromagnetic (AFM) ground states below a Néel temperature of 523 K.[72]

2.2. Construction of Li−M−O Ternary Phase Diagrams and Ground-State Reaction Paths.
Phase diagrams represent the thermodynamic phase equilibria of multicomponent systems and reveal useful insights on the processing and reactions of materials. Nevertheless, the experimental determination of a phase diagram can be extremely time- and labor-consuming which requires dedicated synthesis and characterization of all phases in the target system. Computational tools like DFT can accelerate phase diagram constructions remarkably.[73,74] By calculating the DFT energies of all known compounds in a chemical system, we can determine the $T = 0$ K phase diagram, or ground-state convex hull, of that system. Here in this study, we constructed ternary Li−M−O (M = Co, Ni) convex hulls using the structures with the lowest energy at each composition. The structures were adopted from the Inorganic Crystal Structure Database (ICSD).[75] The reference states (Li, Mn, Ni, and nonsolid O$_2$) were obtained by fitting to experimental data from the SGTE substance database (SSUB) and IIT.[67,69,76−79] Calculations to construct equilibrium Li−M−O (M = Co, Ni) phase diagrams were carried out within the Open Quantum Materials Database (OQMD) framework.[68,69] All the stoichiometries labeled on the phase diagram are part of the ground-state convex hull, indicating that these compounds are stable and have lower energy than any linear combination of other compounds that add up to the same composition. The tie-lines and phase regions in a ternary phase diagram indicate the coexistence of two and three phases, respectively. The equilibrium lithiation/delithiation reaction paths can be determined directly from the ground-state convex hull between Li and MOs which is obtained using a linear programming approach.[73]

2.3. Searching for the Nonequilibrium Phases through the Li-MO Reactions.
Though the equilibrium lithiation pathway can be simply determined from the ground-state convex hull, determining a nonequilibrium reaction pathway is much more difficult, because there is no general, simple guiding principle to determine this pathway. To simulate the nonequilibrium lithiation process (i.e., energetically above the equilibrium reaction pathway) of the MOs, we designed a structure-based, mechanistic method, namely, NEPS (nonequilibrium phase searching method), to search for intermediate phases (Figure 1) by exploring geometrically distinct Li/vacancy configurations on possible insertion sites of MO structures at different compositions (Li/vacancy ratios). NEPS has been successfully applied to predict the energetics and phase evolutions during the lithiation/sodiation process of transition metal sulfides including MoS$_2$,[80] (Cu,Co)$_3$O$_4$,[81] and CuS.[82] An assumption is made on the basis of previous nonequilibrium (de)lithiation studies[18,40] that Li-ion diffusion in the transition metal oxide is significantly faster compared to diffusion of the transition metal ions and oxygen ions during the lithiation reaction. Our hypothesis, therefore, is that Li ion(s) inserted into a compound can find the lowest energy empty site(s) for any given arrangement of transition metals and oxygen ions. The positions of the transition metal ions and oxygen ions respond to the presence of the Li only via local relaxation, enabling the nonequilibrium lithiation process. Our computational method involves the following five steps, described below:

(i) Starting with the host compound (which may or may not contain Li), identify all possible insertion sites. The method is initiated by searching for interstitial sites in the

original transition metal oxide structures. An in-house code MINT (openly available on GitHub)[83−86] was used which automates the search for insertion sites. The algorithm works by placing an analytic, exponential decaying function $[\exp(-r/a)]$ at each atomic site and searching for geometric minima in the resulting function. An illustration of the utility of MINT to find interstitial sites in a complex crystal structure is given in ref 84 for the problem of defects and mass transport in $B_{20}H_{16}$. Models with different sizes of supercell were then built with all the empty insertion sites identified.

(ii) Generate all symmetrically distinct configurations for Li insertion. We worked with the Enum code[87−89] to generate all symmetrically distinct configurations of Li on the unoccupied sites. All configurations were classified according to their composition $Li_x\square_{1-x}MO$.

(iii) Compute total energies of all configurations generated in step ii. To enable a fast energy sampling, simple point-charge electrostatic calculations were conducted, using nominal charge states for the ions in the system.[84]

(iv) Select the structures with lowest electrostatic energies to be computed more accurately and atomically relaxed in DFT. For each composition, the structures were ranked by the electrostatic energies, and the three lowest energy structures were further relaxed using DFT. The formation energies for these selected structures were evaluated according to the following reaction: $MO + xLi^+ \rightarrow Li_xMO$.

(v) Using all of these nonequilibrium structures derived from insertion of Li into the initial TM oxide, build the "nonequilibrium convex hull" and determine phases. For each specific system (Li-MO), we build the corresponding nonequilibrium convex hulls with the calculated formation energies at all compositions. The compositions, structures, and energies located on the convex hull correspond to the identified nonequilibrium phases.

For Co_3O_4, we used a supercell containing 6 Co ions (4 Co^{3+}, 2 Co^{2+}) and 8 O^{2-} ions, which has 16 total tetrahedral and octahedral unoccupied sites that Li ions can insert as shown in Figure 2. As mentioned in the introduction, the lithiation of Co_3O_4 is accompanied by the displacement of tetrahedral Co cations into neighboring empty octahedral sites. We considered the energetic influences on the Co-ion migration to the octahedral site[22] by creating three initial Co_3O_4 configurations, as shown in Figure 3. Figure 3a
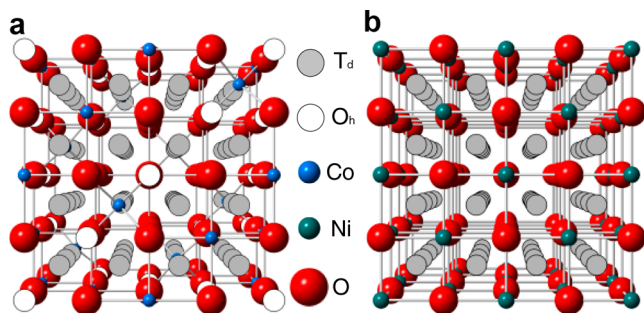

Figure 2. Chemical structures of (a) Co_3O_4 ($Fd\bar{3}m$) and (b) NiO ($R\bar{3}m$). All the unoccupied T_d and O_h sites can be used as an insertion site for lithium ions. The dark blue, green, and red circles represent Co, Ni, and O, respectively, with gray and white circles representing T_d and O_h vacancy sites within the host structure.
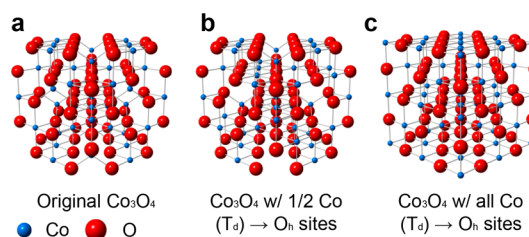

Figure 3. Three initial configurations for the searching of $Li_xCo_3O_4$ nonequilibrium phases. (a) Original Co_3O_4, and (b) Co_3O_4 structure with $1/2$ T_d Co atoms migrated from T_d sites to O_h sites, and (c) disordered Co_3O_4 structure with all T_d Co atoms migrated to O_h sites.

represents the original spinel Co_3O_4 structure (with Co occupying both tetrahedral and octahedral sites in a 1:2 ratio); Figure 3b,c represents structures where half and all of the tetrahedral Co ions are moved to octahedral sites, respectively. Particularly for the $LiCo_3O_4$ phase which is reported to have all Co ions migrated to the octahedral sites randomly, we reproduce the partially disordered structure using the special quasi-random structure (SQS) method by populating the metal sites with Co and Li randomly. An SQS was generated on the basis of a Monte Carlo algorithm implemented in ATAT[54,90−92] with the constraint that the pair and triplet correlation functions of the SQS are identical to those of the statistically random Co/Li population of cation sites at least up to the third nearest neighbor. Starting from these structures shown in Figure 3, we insert the Li atom(s) into the unoccupied octahedral and tetrahedral site(s) for a range of compositions within $0 < x \leq 8$ for $Li_xCo_3O_4$.

For NiO, we used a supercell containing 8 Ni^{2+} ions and 8 O^{2-} ions, which has 16 total tetrahedral unoccupied sites where Li^+ can insert as shown in Figure 2. We insert the Li atom(s) into the unoccupied tetrahedral site(s) in Figure 2b to generate Li_xNiO ($0 < x \leq 2$) structures.

2.4. Derivation of Voltage Profiles. In a two-phase reaction between Li_yMO and Li_xMO

$$Li_xMO + (y - x)Li \rightarrow Li_yMO \qquad (1)$$

The average lithiation/delithiation reaction voltage relative to Li/Li^+ is given by the negative of the reaction free energy per Li as shown by Equation 2.[93]

$$V = \frac{\Delta G_f}{F\Delta N_{Li}} \qquad (2)$$

Here, F is the Faraday constant, $\Delta N_{Li} = y - x$ is the amount of Li added/removed, and ΔG_f is the (molar) change in free energy of the reaction. The enthalpic (pV_m) contribution to G is of order 10 μeV per Li at atmospheric pressure and can be safely ignored.[15] In the following, we approximated G in eq 1 with $T = 0$ K total energies (E) from DFT calculations neglecting the entropic contributions.

$$\Delta E = E(Li_yMO) - E(Li_xMO) - (y - x)E(Li_{metal}) \qquad (3)$$

Here, $E(Li_xMO)$ and $E(Li_yMO)$ generically represent the sum of the total energies of all product phases or reactant phases at the specified stoichiometry, as shown in Table 1. Of course, experimental lithiation/delithiation reactions do not necessarily proceed strictly through a series of two-phase reactions (the latter is an artifact of using strictly $T = 0$ K convex hull constructions). Thus, the voltage profiles obtained should be viewed as approximate, and very small voltage steps should not

Table 1. Lithiation Reactions of the Equilibrium Path of Co_3O_4 and NiO

region	reaction	capacity [mA h/g]	voltage [V]
	Co_3O_4		
I	$Co_3O_4 + Li \rightarrow LiCoO_2 + 2CoO$	111	2.53
II	$LiCoO_2 + 2CoO + Li \rightarrow 1/3Li_6CoO_4 + 8/3CoO$	223	1.82
V	$1/3Li_6CoO_4 + 8/3CoO + 4Li \rightarrow Li_6CoO_4 + 2Co$	668	1.81
IV	$Li_6CoO_4 + 2Co + 2Li \rightarrow 4Li_2O + 3Co$	890	1.66
	NiO		
I	$NiO + Li \rightarrow 1/2Li_2NiO_2 + 1/2Ni$	359	1.75
II	$1/2Li_2NiO_2 + 1/2Ni + 1Li \rightarrow Li_2O + Ni$	718	1.71

be taken as significant.[15] Small voltage drops in the voltage profile would become much more rounded or even completely smoothed into a continuous curve at finite temperatures (i.e., room temperature) when entropic contributions are taken into account.[56]

3. RESULTS

3.1. Li−M−O (M = Co, Ni) Ground-State Convex Hulls and Equilibrium (De)lithiation Voltage Profiles. We begin with the calculation of equilibrium (de)lithiation pathways, given by the equilibrium convex hull construction. The ternary Li−Co−O and Li−Ni−O ground-state convex hulls are presented in Figure 4 with stable compositions marked by
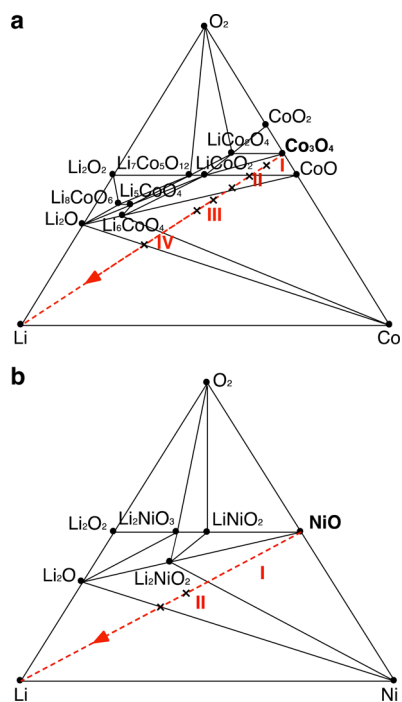

Figure 4. Li−M−O phase diagrams and equilibrium lithiation/delithiation paths of (a) Co_3O_4 and (b) NiO. The equilibrium reaction paths are represented by the dotted line. The three-phase regions which the lithiation/delithiation path goes through are marked by Roman numerals. Compositions marked with an × are the nonequilibrium phases identified in Section 3.2.

filled circles. Stability of compounds on the convex hull indicates that they have a lower DFT energy than any linear combination of other compounds (which are contained in the OQMD database). Compositions marked with an × are the nonequilibrium phases identified in Section 2.3 inside a stable three-phase region or on the two-phase tie-line which have

higher energy than a mixture of the three/two compounds that define the triangle/tie-line. Although such compounds are thermodynamically unstable, they can be nonequilibrium if kinetic limitations (e.g., diffusion, nucleation) prevent the relaxation of the system to the equilibrium, stable phases.[13]

The equilibrium lithiation reaction paths of MOs go through multiple three-phase regions in Figure 4 consisting of the stable phases marked in our ternary phase diagrams. These regions correspond to various lithiation reactions listed in Table 1, where we calculate the capacities and average voltages of these reactions. In Figure 3, we compare the equilibrium reaction voltage profiles predicted with DFT with the experimental voltage profiles adapted from refs 6, 7, and 94. We note that the overall values of the calculated equilibrium voltage profiles of Co_3O_4 and NiO with DFT reasonably agree with the experimental delithiation curves (Figure 5a,b). Therefore, we
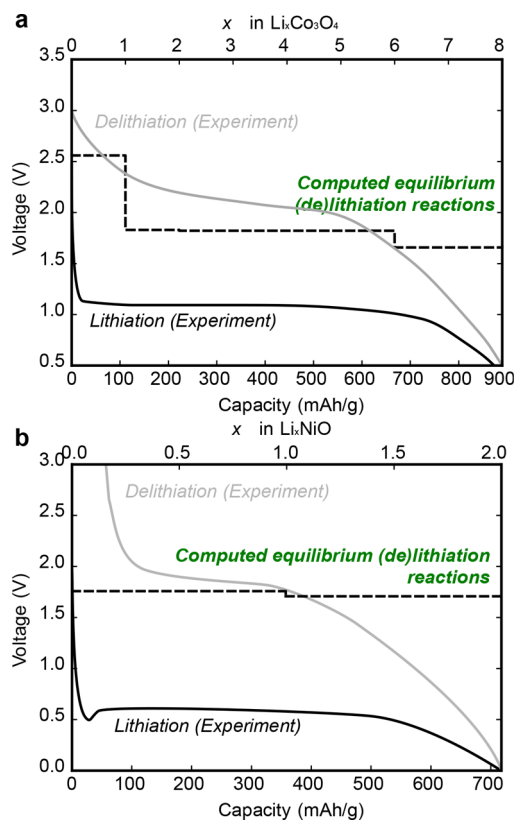

Figure 5. Calculated equilibrium lithiation/delithiation voltage profiles for (a) Co_3O_4 and (b) NiO and experimental voltage profiles adapted from refs 6, 7, and 94. The overall values of the calculated equilibrium voltage profiles of Co_3O_4 and NiO reasonably agree with the experimental delithiation curves. The experimental lithiation/delithiation profiles are represented by the black and gray curves.

conclude that the delithiation of $Li_8Co_3O_4$ ($4Li_2O \cdot 3Co$) and Li_2NiO ($Li_2O \cdot Ni$) follows pathways which are energetically close to the equilibrium reaction processes (further discussed in Section 3.4). There is a voltage difference between the calculated equilibrium profile and experimental curve at the beginning of the delithiation. Many factors (e.g., entropy, reaction kinetics, compositional inhomogeneity, etc.) can contribute to this voltage difference, yet a detailed investigation on clarifying the energetically dominant factor is beyond our current scope. However, for Co_3O_4 and NiO, the calculated equilibrium voltage profiles are much higher compared to the lithiation plateaus at 1.1/0.7 V as shown in Figure 3a,b. These voltage differences reflect the large voltage hysteresis during the cycling of Co_3O_4 and NiO and suggest an alternative reaction path for the lithiation processes. As a result, we focus on the nonequilibrium lithiation pathways involving intermediate structures as an explanation of the discrepancies between experimental lithiation and calculated equilibrium voltages.

3.2. Nonequilibrium Lithiation Voltage Profiles. Since the lithiation voltages from experiments exhibit large differences with the equilibrium voltage profile (Figure 5), we investigate the nonequilibrium lithiation process of MOs by the prediction of nonequilibrium structures and reaction pathways based on geometrical enumerations (the methodology is detailed in Section 2.3). During the lithiation process of Co_3O_4 and NiO, we identify several nonequilibrium phases ($Li_xCo_3O_4$, $x = 1, 2, 3, 4, 5, 8$; and Li_xNiO, $x = 1.625, 2$) along the $Li–Co_3O_4(NiO)$ "non-equilibrium convex hulls" as shown in Figure 6a,c. Using these nonequilibrium phases, the overall voltages of calculated "non-equilibrium" lithiation reactions (Figure 4b,d) are in significantly better agreement with experimental lithiation voltages than the calculated equilibrium values.[6,7] Because our voltages are based on $T = 0$ K energetics, the shape of the calculated voltage profile is a series of constant voltage reactions with steps in between. However, the experimental curves are generally more smooth and continuous. It is noteworthy that the simulated voltage profiles will generally become more smooth when entropic considerations and finite temperature[56] are taken into account. The comparison of calculated voltages and structural information with experiment [electrochemical, XRD, and EXAFS (extended X-ray absorption fine structure method)] led us to the conclusion that the lithiation of Co_3O_4 and NiO follows a series of nonequilibrium phases instead of the ground-state equilibrium phases in Table 1. The structural validation and comparison with experiment will be discussed in following sections. Additionally, discharge voltage curves of certain conversion-type materials could be affected by many different experimental aspects, including synthesis method, particle morphology, test settings, etc. Particularly for Co_3O_4 and NiO, the lithiation voltage profiles of various nano-particles[37,38,95−97] demonstrate continuously decreasing trends in contrast to the largely flat profile obtained using bulk materials as shown in Figure 6. However, exploring for the detailed reasons behind these nanoparticles vs bulk experimental voltage curves is beyond the scope of this study.

3.3. Atomistic Structural Evolutions during the Non-equilibrium Lithiation Process. *3.3.1. Co_3O_4.* We next look into the atomistic phase evolution during the nonequilibrium lithiation process. The lithiation of Co_3O_4 starts with both Li and Co (migrated from the T_d sites) taking the unoccupied O_h sites. As all the O_h sites are fully occupied by Li and Co at $x = 1$; the resulting $LiCo_3O_4$ phase adopts a partially disordered (Li/Co) rocksalt structure (Figure 7b), as observed by
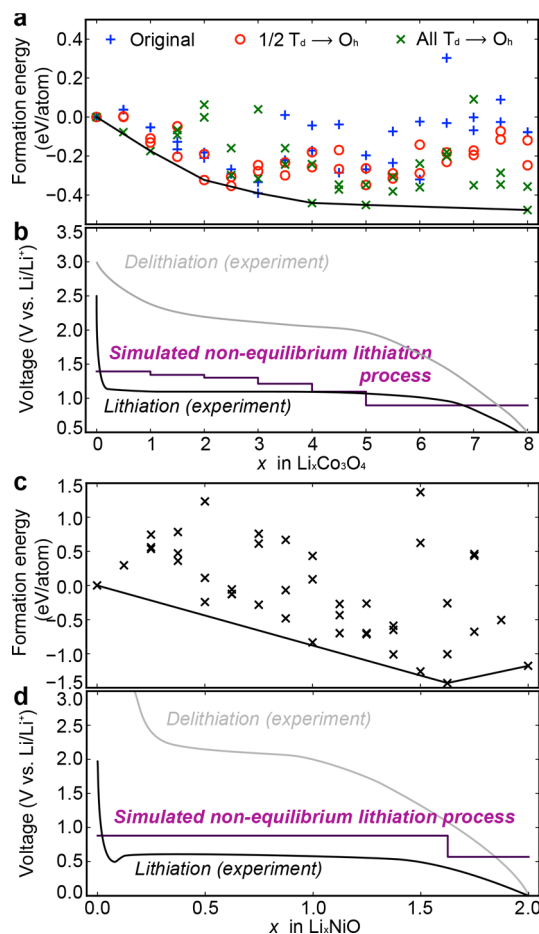

Figure 6. Convex hulls generated with all the calculated non-equilibrium phases for (a) Co_3O_4 and (b) NiO, and the corresponding voltage profiles of the Li insertion into (c) Co_3O_4 and (d) NiO. Predicted nonequilibrium reaction voltage profiles fall into the experimental lithiation voltage intervals.

Thackeray et al. through X-ray diffraction analysis.[22] In the following step ($x = 2$) in Figures 7c, continuing Li-ion insertion forces the octahedrally coordinated cobalt ions in $LiCo_3O_4$ to migrate back to tetrahedral sites in $Li_2Co_3O_4$. A mosaic structure (Figure 7c) forms at this step with localized CoO−Li_2O character, and Co ions occupy both the T_d site and O_h sites confirming the X-ray diffraction analysis conducted for $Li_{1.92}Co_3O_4$ by Thackeray et al.[22] With further Li intercalation ($x = 3$), we observe in Figures 7c that the oxygen fcc frameworks still stay intact. To better understand the atomistic reduction of ions in the cells, we conduct Bader charge analysis[98,99] for Co ions in intermediate phases (Figure 8a). We also monitor the interatomic distance between selected nearest neighbor ions through the lithiation process, as shown in Figure 8b. From Co_3O_4 to $Li_3Co_3O_4$, the Bader charge of Co decreases for $−0.44e$ indicating the Co-ion reduction ($Co^{3+} \rightarrow Co^{2+}$). Co−Co and O−O interatomic distances in Figure 8b show limited changes indicating the overall preservation of the backbone of the structure. These observations indicate the potential to use Co_3O_4 as a reversible, intercalation-type electrode in a constrained lithiation range ($0 < x < 3$).

Beyond the intercalation-type reaction ($x \geq 4$), Co ions start to get partially reduced to their metallic oxidation state ($Co^{2+} \rightarrow Co^0$, Figure 8a) and begin to be extruded from the structure. Co ions in these nonequilibrium structures begin to cluster, and
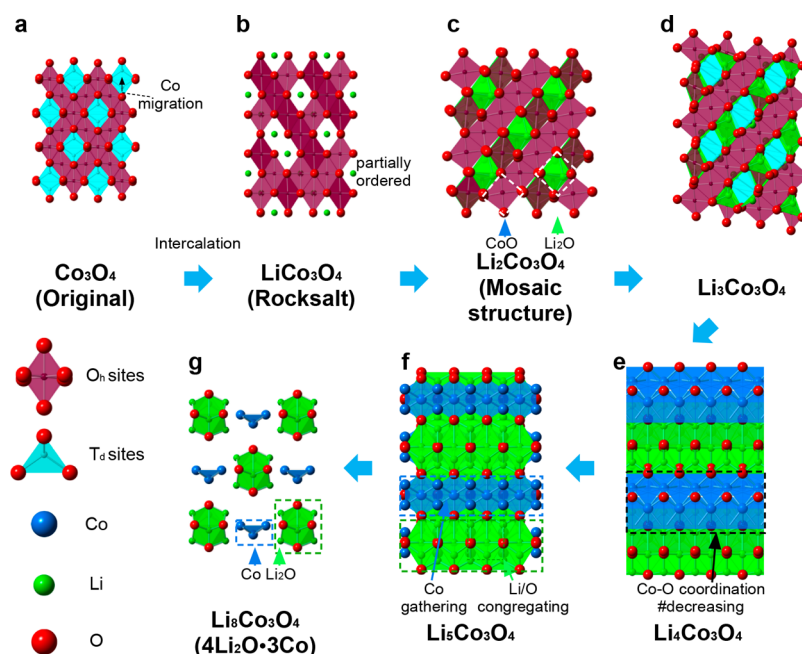
Figure 7. Structures of the nonequilibrium phases on the convex hull and the corresponding phase evolution. At the beginning of the lithiation, both inserted Li and Co ions from the T_d sites tend to occupy the empty O_h sites forming $LiCo_3O_4$ as shown in part b (Co movements are indicated by black arrows). Furthermore, it is observed that the oxygen fcc array starts to be distorted in part c. In $Li_4Co_3O_4$, the Co−O coordination numbers are decreasing (labeled by the green rectangle) in part e, followed by the Li/O congregating (green rectangle) and Co gathering (blue square) in part f. Lastly, we observe the formation of Li_2O and Co clusters, i.e., a strong tendency to phase separate into ground-state phases at that composition, which is consistent with previous experiments.[7,29]
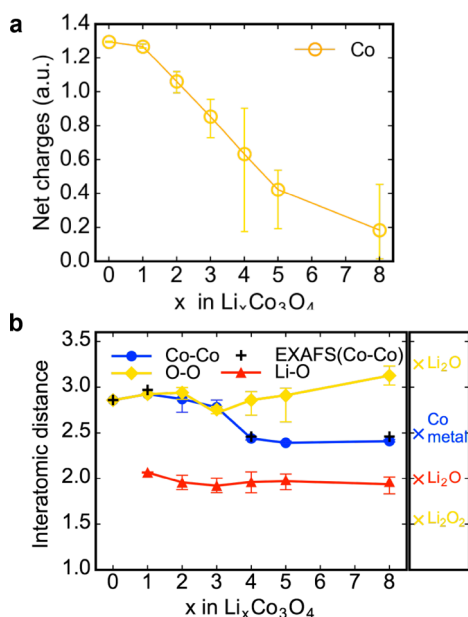

Figure 8. (a) Averaged net charges on Co in $Li_xCo_3O_4$, ($0 < x < 8$) based on the Bader charge analysis. The error bar corresponds to the distribution (maximum and minimum) of charges on the Co ion. (b) Interatomic distance during the lithiation process of Co_3O_4. The error bar corresponds to the distribution (maximum and minimum) of interatomic distances. EXAFS data on Co−Co interatomic distance is adapted from refs 25 and 100. Typical interatomic bond lengths (adapted from refs 103 and 104) are also provided in the figure (right).

Li/O also starts to congregate as the system approaches the $x = 5$ $Li_5Co_3O_4$ phase in Figure 7f. The lithiation now starts to resemble a pathway closer to the conversion-type reaction.

When the Co_3O_4 is fully lithiated ($x = 8$), Co ions have been fully reduced to Co metal, and Li ions combine with O ions to form a distorted Li_2O. We observe that, in this highly lithiated state, the Co clusters distribute in an alternate layer of distorted Li_2O in Figure 7g, which is an indication of the phase separation tendency between nanoscale Co metal and lithia. We consistently observe that the distances between neighboring Li−O and O−O ions in Figure 8 approach the typical bond lengths in Li_2O while the Co−Co distances get close to that of Co metal, which validates the experimental observation of Co nanoparticles dispersed in the disordered Li_2O in previous studies.[7,29] Our results have demonstrated that only Li_2O is forming and no other products such as Li_2O_2 or LiO_2 are observed during the lithiation process (Figure 8b). We have compared our calculated Co−Co interatomic distances during lithiation with the values measured by extended X-ray absorption fine structure method (EXAFS).[25,100] The predicted Co−Co distance shows reasonable agreement with the experimental EXAFS observations across a range of Li concentrations, further validating our lithiation pathway results (Figure 8b).

3.3.2. NiO. Unlike Co_3O_4, the lithiation of NiO starts with conversion-type features. When lithiation begins, Li ions go into the T_d interstitial sites of the NiO structure (Figure 9). After 1.6 Li are inserted, Ni^{2+} ions have been largely reduced to Ni^0 metal atoms as shown by Bader charge analysis (Figure 10a). Additionally, the system reaches its first nonequilibrium phase characterized by alternative layers of distorted Ni and lithia. The variation of Ni−Ni interatomic distance as a function of x in Figure 9b confirms the changes in the oxidation state of Ni ($Ni^{2+} \rightarrow Ni^0$). Some of the Ni ions are still bonded with oxygen ions with a narrow distance between them (Figure 10b). When 2 Li are inserted, all the Ni ions are reduced to Ni^0 with lithia forming single layers implying the phase separation
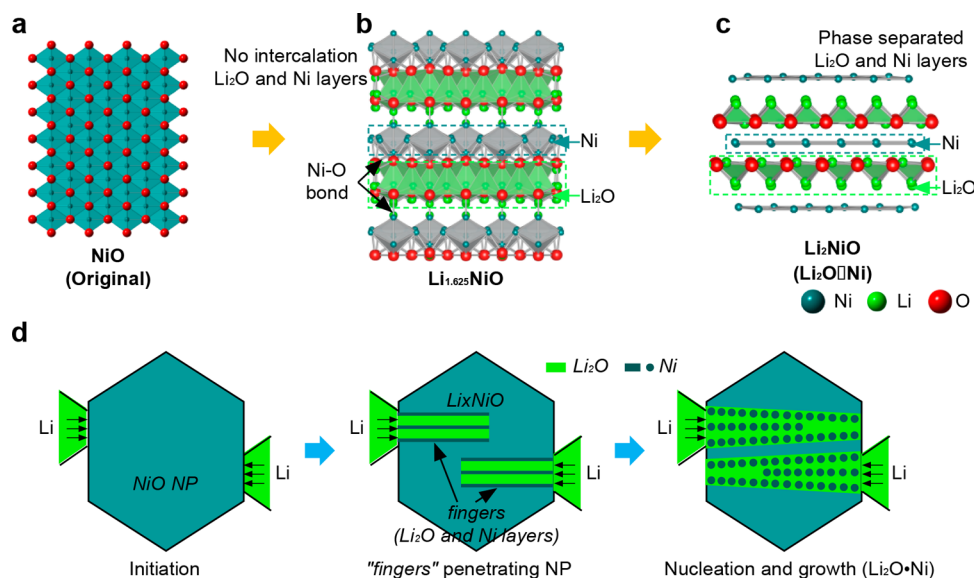
Figure 9. Structures of the two nonequilibrium phases on the convex hull and schematic illustration of the "finger" lithiation mechanism of NiO.[28] The lithiation of NiO starts with conversion-type features, and Li ions go into the T_d interstitial sites of the NiO structure. After 1.625 Li are inserted, Ni^{2+} ions have been partially reduced to the Ni^0 metal atoms. The system reaches the first nonequilibrium phase characterized by alternative layers of distorted Ni and lithia shown in part b. Some of the Ni ions are still bonded with oxygen ions with the narrow distance between them. When the 2 Li are inserted, all the Ni ions get reduced by Li with lithia structures becoming more regular and Ni metal atoms forming single layers implying the phase separation between nanoscale Ni metal and lithia (c). The nonequilibrium phases featured with alternative layers of lithia and Ni can be used to explain the "finger" lithiation mode of NiO.
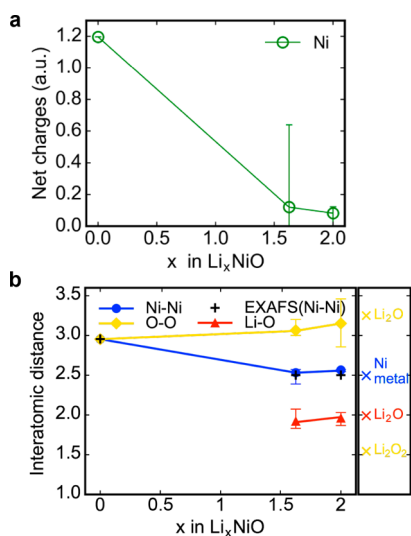

Figure 10. (a) Averaged net charges on Ni in Li_xNiO ($0 < x < 2$) based on the Bader charge analysis. The error bar corresponds to the distribution (maximum and minimum) of charges on the Ni ion. (b) Interatomic distance during the lithiation process of NiO. The error bar corresponds to the distribution (maximum and minimum) of interatomic distances. EXAFS data on Ni−Ni interatomic distance is adapted from ref [41]. Typical interatomic bond lengths (adapted from refs [103], and [104]) are also provided in the figure (right).

between nanoscale Ni metal and lithia (Figure 9c). Again, only Li_2O is formed, and no other products such as Li_2O_2 or LiO_2 are observed during the lithiation process (Figure 10b). Similar to Co_3O_4, the predicted Ni−Ni distance shows remarkable agreement with the experimental observations as a function of Li concentration (Figure 10b).[41] Using *in situ* TEM observations,[28] He et al. reported the lithiation of NiO penetrates into the material through a "fingerlike" morphology.

The lithiation "fingers" that propagate into the sample are in the form of high-aspect-ratio lithia and Ni^0 layers, and our nonequilibrium pathway calculations feature precisely this type of morphology and hence help explain the experimental observations. Here we propose that the development of the fingers is enabled by the formation and growth of the nonequilibrium intermediate phases Li_xNiO ($1.625 < x < 2.0$) featured with lithia and Ni metal layers. The experimental identification of the nonequilibrium intermediate phases is under investigation.[101]

3.4. Discussion. As described above in Sections 3.2 and 3.3, the final nonequilibrium phases after full lithiation of Co_3O_4 and NiO are composed of nanoscale Co, Ni, and Li_2O clusters, and we assert that the reverse delithiation process will proceed at a potential closer to the equilibrium voltage profile. Since the $Co/Ni/Li_2O$ clusters are very closely integrated into the nanoscale with high interfacial area, they will still be at a higher energetic state compared with the bulk phase (where these clusters can exist on a much larger length scale with lower interfacial energy). Once the electrode is fully delithiated back to the original Co_3O_4 or NiO structure, the nonequilibrium lithiation process will start again. By determination of the lithiation/delithiation reaction paths, our theoretical study now provides an insight into the large voltage hysteresis observed during the cycling of Co_3O_4 and NiO.[6,7,29] The distinct reaction pathways between the lithiation and delithiation process induce the large voltage hysteresis.

Specifically, during the lithiation of Co_3O_4, the oxygen fcc frameworks start to collapse after four Li ions are inserted ($x \geq 4$), as displayed in Figure 7e. We hypothesize that if only 3 lithium units are inserted into the Co_3O_4 electrode, the lithiation process may proceed as an intercalation reaction with the oxygen backbone still preserved yet with Co migration in the structure, which may offer an enhanced cyclability with a capacity of ~334 mA h/g and much more constrained volume

expansion. It is also possible that the following delithiation process may proceed with the intercalation-type reaction that may prevent the voltage hysteresis and particle cracking.

There have been studies using the confinement of multiple nanoscale NiO layers within an electrode to direct lithium transport and reactivity.[26,102] The layered features of the nonequilibrium phases predicted in this work (Figure 9b,c) during the lithiation of NiO rationalize the design of the multi-nano-layer electrode and also offer guidance on its further improvement. With the advancement of the synthesis at the nanoscale, we assert that enhanced reactivity and reversibility could be achieved when the single NiO layer thickness approaches the counterpart of Ni/Li_2O dual layers in our computed nonequilibrium phases (~ 10 Å). In this case, the corresponding (de)lithiation would therefore require only Li-, Ni-, and O-ion migration within extremely limited length scales and only in a layered morphology, showing the possible use of these nanoscale materials as a fast-rate electrode material.

4. CONCLUSION

We have combined first-principles calculations of equilibrium and nonequilibrium structures derived from the original MO (Co_3O_4, NiO) structures to explain the underlying mechanisms of lithiation and delithiation of these conversion electrodes in Li-ion batteries. A structure-based method was designed to search for nonequilibrium intermediate phases by exploring geometrically distinct Li/vacancy configurations on possible insertion sites of MO structures at different compositions (Li/vacancy ratios). For Co_3O_4 and NiO, the overall value of equilibrium voltage profiles (~ 2.1 and 1.74 V) reasonably agree with the experimental delithiation voltages; however, they show large deviations from the experimental lithiation counterparts (~ 1.1 and 1.2 V) reflecting the large voltage hysteresis during cycling. We focus on the voltage deviations caused by the nonequilibrium lithiation process by searching for possible nonequilibrium phases that appear in the lithiation reactions. For Co_3O_4, we have identified nonequilibrium phases where the first three phases ($x = 1$, 2, and 3) preserve a nearly rigid oxygen fcc framework. Therefore, we assert that Co_3O_4 should have enhanced reversibility as an electrode when the charge/discharge is limited to 3 mol of Li per formula unit or less. Even with this restriction, this material could offer better cyclability at a reasonable capacity of ~ 334 mA h/g. For NiO, we have identified nonequilibrium phases (Li_xNiO, $x = 1.625$ and 2) both of which are characterized by alternative layers of distorted Ni and lithia. The overall voltages of calculated lithiation/delithiation profiles using energetics of these nonequilibrium/equilibrium phases show good agreement with experimental voltages and explain the large voltage hysteresis during Co_3O_4/NiO cycling. Our study provides new insights on the lithiation process of transition metal oxides and could help future experiments to overcome the current limitations of the conversion-type electrode materials promoting the development of more advanced LIBs.

■ AUTHOR INFORMATION

Corresponding Author
*E-mail: c-wolverton@northwestern.edu.

ORCID
Jinsong Wu: 0000-0002-7305-7927
Jiangang He: 0000-0001-9643-3617
Chris Wolverton: 0000-0003-2248-474X

Present Address
§(M.A.) Toyota Research Institute, 4440 El Camino Real, Los Altos, California 94022, United States.

Notes
The authors declare no competing financial interest.

■ REFERENCES

(1) Thackeray, M. M.; Wolverton, C.; Isaacs, E. D. Electrical Energy Storage for Transportation-Approaching the Limits Of, and Going Beyond, Lithium-Ion Batteries. *Energy Environ. Sci.* **2012**, *5*, 7854−7863.

(2) Mizushima, K.; Jones, P. C.; Wiseman, P. J.; Goodenough, J. B. LixCoO2 (0 < x < 1):A New Cathode Material for Batteries of High Energy Density. *Mater. Res. Bull.* **1980**, *15*, 783−789.

(3) Padhi, A. K.; Nanjundaswamy, K. S.; Goodenough, J. B. Phospho-Olivines as Positive-Electrode Materials for Rechargeable Lithium Batteries. *J. Electrochem. Soc.* **1997**, *144*, 1188−1194.

(4) Chan, C. K.; Peng, H.; Liu, G.; McIlwrath, K.; Zhang, X. F.; Huggins, R. A.; Cui, Y. High-Performance Lithium Battery Anodes Using Silicon Nanowires. *Nat. Nanotechnol.* **2008**, *3*, 31−35.

(5) Derrien, G.; Hassoun, J.; Panero, S.; Scrosati, B. Nanostructured Sn−C Composite as an Advanced Anode Material in High-Performance Lithium-Ion Batteries. *Adv. Mater.* **2007**, *19*, 2336−2340.

(6) Poizot, P.; Laruelle, S.; Grugeon, S.; Dupont, L.; Tarascon, J. M. Nano-Sized Transition-Metal Oxides as Negative-Electrode Materials for Lithium-Ion Batteries. *Nature* **2000**, *407*, 496−499.

(7) Badway, F.; Plitz, I.; Grugeon, S.; Laruelle, S.; Dollé, M.; Gozdz, A. S.; Tarascon, J.-M. Metal Oxides as Negative Electrode Materials in Li-Ion Cells. *Electrochem. Solid-State Lett.* **2002**, *5*, A115−A118.

(8) Khatib, R.; Dalverny, A.-L.; Saubanère, M.; Gaberscek, M.; Doublet, M.-L. Origin of the Voltage Hysteresis in the CoP Conversion Material for Li-Ion Batteries. *J. Phys. Chem. C* **2013**, *117*, 837−849.

(9) Meggiolaro, D.; Gigli, G.; Paolone, A.; Reale, P.; Doublet, M. L.; Brutti, S. Origin of the Voltage Hysteresis of MgH2 Electrodes in Lithium Batteries. *J. Phys. Chem. C* **2015**, *119*, 17044−17052.

(10) Li, L.; Jacobs, R.; Gao, P.; Gan, L.; Wang, F.; Morgan, D.; Jin, S. Origins of Large Voltage Hysteresis in High-Energy-Density Metal Fluoride Lithium-Ion Battery Conversion Electrodes. *J. Am. Chem. Soc.* **2016**, *138*, 2838−2848.

(11) Delacourt, C.; Poizot, P.; Tarascon, J.-M.; Masquelier, C. The Existence of a Temperature-Driven Solid Solution in LixFePO4 for 0 ≤ X ≤ 1. *Nat. Mater.* **2005**, *4*, 254−260.

(12) Malik, R.; Zhou, F.; Ceder, G. Kinetics of Non-Equilibrium Lithium Incorporation in LiFePO4. *Nat. Mater.* **2011**, *10*, 587−590.

(13) Singer, A.; Ulvestad, A.; Cho, H.-M.; Kim, J. W.; Maser, J.; Harder, R.; Meng, Y. S.; Shpyrko, O. G. Nonequilibrium Structural Dynamics of Nanoparticles in LiNi(1/2)Mn(3/2)O4 Cathode under Operando Conditions. *Nano Lett.* **2014**, *14*, 5295−5300.

(14) Doe, R. E.; Persson, K. A.; Meng, Y. S.; Ceder, G. First-Principles Investigation of the Li−Fe−F Phase Diagram and Equilibrium and Nonequilibrium Conversion Reactions of Iron Fluorides with Lithium. *Chem. Mater.* **2008**, *20*, 5274−5283.

(15) Chan, M. K. Y.; Wolverton, C.; Greeley, J. P. First Principles Simulations of the Electrochemical Lithiation and Delithiation of Faceted Crystalline Silicon. *J. Am. Chem. Soc.* **2012**, *134*, 14362−14374.

(16) Bazant, M. Z. Theory of Chemical Kinetics and Charge Transfer Based on Nonequilibrium Thermodynamics. *Acc. Chem. Res.* **2013**, *46*, 1144−1160.

(17) Jain, A.; Ong, S. P.; Hautier, G.; Chen, W.; Richards, W. D.; Dacek, S.; Cholia, S.; Gunter, D.; Skinner, D.; Ceder, G.; Persson, K. A. Commentary: The Materials Project: A Materials Genome Approach to Accelerating Materials Innovation. *APL Mater.* **2013**, *1*, 11002.

(18) Chang, D.; Chen, M.-H.; Van der Ven, A. Factors Contributing to Path Hysteresis of Displacement and Conversion Reactions in Li Ion Batteries. *Chem. Mater.* **2015**, *27*, 7593−7600.

(19) Kim, H.; Kim, H.; Kim, H.; Kim, J.; Yoon, G.; Lim, K.; Yoon, W.-S.; Kang, K. Understanding Origin of Voltage Hysteresis in Conversion Reaction for Na Rechargeable Batteries: The Case of Cobalt Oxides. *Adv. Funct. Mater.* **2016**, *26*, 5042−5050.

(20) Malini, R.; Uma, U.; Sheela, T.; Ganesan, M.; Renganathan, N. G. Conversion Reactions: A New Pathway to Realise Energy in Lithium-Ion Battery—review. *Ionics* **2009**, *15*, 301−307.

(21) Cabana, J.; Monconduit, L.; Larcher, D.; Palacín, M. R. Beyond Intercalation-Based Li-Ion Batteries: The State of the Art and Challenges of Electrode Materials Reacting Through Conversion Reactions. *Adv. Mater.* **2010**, *22*, E170−E192.

(22) Thackeray, M.; Baker, S.; Adendorff, K.; Goodenough, J. Lithium Insertion into Co3O4: A Preliminary Investigation. *Solid State Ionics* **1985**, *17*, 175−181.

(23) Kang, Y.-M.; Kim, K.-T.; Lee, K.-Y.; Lee, S.-J.; Jung, J.-H.; Lee, J.-Y. Improvement of Initial Coulombic Efficiency of Co3O4 by Ballmilling Using Ni as an Additive. *J. Electrochem. Soc.* **2003**, *150*, A1538−A1543.

(24) Needham, S. A.; Wang, G. X.; Konstantinov, K.; Tournayre, Y.; Lao, Z.; Liu, H. K. Electrochemical Performance of Co3O4−C Composite Anode Materials. *Electrochem. Solid-State Lett.* **2006**, *9*, A315−A319.

(25) Connor, P. A.; Irvine, J. T.S Combined X-Ray Study of Lithium (Tin) Cobalt Oxide Matrix Negative Electrodes for Li-Ion Batteries. *Electrochim. Acta* **2002**, *47*, 2885−2892.

(26) Wang, Y.; Qin, Q.-Z. A Nanocrystalline NiO Thin-Film Electrode Prepared by Pulsed Laser Ablation for Li-Ion Batteries. *J. Electrochem. Soc.* **2002**, *149*, A873−A878.

(27) Larcher, D.; Sudant, G.; Leriche, J.-B.; Chabre, Y.; Tarascon, J.-M. The Electrochemical Reduction of Co3O4 in a Lithium Cell. *J. Electrochem. Soc.* **2002**, *149*, A234−A241.

(28) He, K.; Xin, H. L.; Zhao, K.; Yu, X.; Nordlund, D.; Weng, T.-C.; Li, J.; Jiang, Y.; Cadigan, C. A.; Richards, R. M.; Doeff, M. M.; Yang, X.-Q.; Stach, E. A.; Li, J.; Lin, F.; Su, D. Transitions from Near-Surface to Interior Redox upon Lithiation in Conversion Electrode Materials. *Nano Lett.* **2015**, *15*, 1437−1444.

(29) Poizot, P.; Laruelle, S.; Grugeon, S.; Tarascon, J.-M. Rationalization of the Low-Potential Reactivity of 3d-Metal-Based Inorganic Compounds toward Li. *J. Electrochem. Soc.* **2002**, *149*, A1212−A1217.

(30) Wang, G. X.; Chen, Y.; Konstantinov, K.; Yao, J.; Ahn, J.; Liu, H. K.; Dou, S. X. Nanosize Cobalt Oxides as Anode Materials for Lithium-Ion Batteries. *J. Alloys Compd.* **2002**, *340*, L5−L10.

(31) Kang, Y.-M.; Song, M.-S.; Kim, J.-H.; Kim, H.-S.; Park, M.-S.; Lee, J.-Y.; Liu, H. K.; Dou, S. X. A Study on the Charge−discharge Mechanism of Co3O4 as an Anode for the Li Ion Secondary Battery. *Electrochim. Acta* **2005**, *50*, 3667−3673.

(32) Rollmann, G.; Gruner, M. E.; Hucht, A.; Meyer, R.; Entel, P.; Tiago, M. L.; Chelikowsky, J. R. Shellwise Mackay Transformation in Iron Nanoclusters. *Phys. Rev. Lett.* **2007**, *99*, 083402−083405.

(33) Wang, F.; Yu, H.-C.; Chen, M.-H.; Wu, L.; Pereira, N.; Thornton, K.; Van der Ven, A.; Zhu, Y.; Amatucci, G. G.; Graetz, J. Tracking Lithium Transport and Electrochemical Reactions in Nanoparticles. *Nat. Commun.* **2012**, *3*, 1201−1208.

(34) Lou, X. W.; Deng, D.; Lee, J. Y.; Feng, J.; Archer, L. A. Self-Supported Formation of Needlelike Co3O4 Nanotubes and Their Application as Lithium-Ion Battery Electrodes. *Adv. Mater.* **2008**, *20*, 258−262.

(35) Li, Y.; Tan, B.; Wu, Y. Freestanding Mesoporous Quasi-Single-Crystalline CO3O4 Nanowire Arrays. *J. Am. Chem. Soc.* **2006**, *128*, 14258−14259.

(36) Wang, X.; Wu, X.-L.; Guo, Y.-G.; Zhong, Y.; Cao, X.; Ma, Y.; Yao, J. Synthesis and Lithium Storage Properties of Co3O4 Nanosheet-Assembled Multishelled Hollow Spheres. *Adv. Funct. Mater.* **2010**, *20*, 1680−1686.

(37) Wu, Z.-S.; Ren, W.; Wen, L.; Gao, L.; Zhao, J.; Chen, Z.; Zhou, G.; Li, F.; Cheng, H.-M. Graphene Anchored with Co3O4 Nanoparticles as Anode of Lithium Ion Batteries with Enhanced Reversible Capacity and Cyclic Performance. *ACS Nano* **2010**, *4*, 3187−3194.

(38) Varghese, B.; Reddy, M. V.; Yanwu, Z.; Lit, C. S.; Hoong, T. C.; Subba Rao, G. V.; Chowdari, B. V. R.; Wee, A. T. S.; Lim, C. T.; Sow, C.-H. Fabrication of NiO Nanowall Electrodes for High Performance Lithium Ion Battery. *Chem. Mater.* **2008**, *20*, 3360−3367.

(39) Hosono, E.; Fujihara, S.; Honma, I.; Zhou, H. The High Power and High Energy Densities Li Ion Storage Device by Nanocrystalline and Mesoporous Ni/NiO Covered Structure. *Electrochem. Commun.* **2006**, *8*, 284−288.

(40) Yu, H.-C.; Ling, C.; Bhattacharya, J.; Thomas, J. C.; Thornton, K.; Van der Ven, A. Designing the next Generation High Capacity Battery Electrodes. *Energy Environ. Sci.* **2014**, *7*, 1760−1768.

(41) Boesenberg, U.; Marcus, M. A.; Shukla, A. K.; Yi, T.; McDermott, E.; Teh, P. F.; Srinivasan, M.; Moewes, A.; Cabana, J. Asymmetric Pathways in the Electrochemical Conversion Reaction of NiO as Battery Electrode with High Storage Capacity. *Sci. Rep.* **2015**, *4*, 7133−7141.

(42) Ponrouch, A.; Cabana, J.; Dugas, R.; Slack, J. L.; Palacín, M. R. Electroanalytical Study of the Viability of Conversion Reactions as Energy Storage Mechanisms. *RSC Adv.* **2014**, *4*, 35988−35996.

(43) Van der Ven, A.; Aydinol, M. K.; Ceder, G.; Kresse, G.; Hafner, J. First-Principles Investigation of Phase Stability in LixCoO2. *Phys. Rev. B: Condens. Matter Mater. Phys.* **1998**, *58*, 2975−2987.

(44) Ceder, G.; Chiang, Y.-M.; Sadoway, D. R.; Aydinol, M. K.; Jang, Y.-I.; Huang, B. Identification of Cathode Materials for Lithium Batteries Guided by First-Principles Calculations. *Nature* **1998**, *392*, 694−696.

(45) Morgan, D.; Van der Ven, A.; Ceder, G. Li Conductivity in LixMPO4 (M = Mn, Fe, Co, Ni) Olivine Materials. *Electrochem. Solid-State Lett.* **2004**, *7*, A30−A32.

(46) Kang, K.; Meng, Y. S.; Bréger, J.; Grey, C. P.; Ceder, G. Electrodes with High Power and High Capacity for Rechargeable Lithium Batteries. *Science (Washington, DC, U. S.)* **2006**, *311*, 977−980.

(47) Meng, Y. S.; Arroyo-de Dompablo, M. E. First Principles Computational Materials Design for Energy Storage Materials in Lithium Ion Batteries. *Energy Environ. Sci.* **2009**, *2*, 589−609.

(48) Kim, S.; Aykol, M.; Wolverton, C. Surface Phase Diagram and Stability of (001) and (111) LiMn2O4 Spinel Oxides. *Phys. Rev. B: Condens. Matter Mater. Phys.* **2015**, *92*, 115411−115420.

(49) Jaber-Ansari, L.; Puntambekar, K. P.; Kim, S.; Aykol, M.; Luo, L.; Wu, J.; Myers, B. D.; Iddir, H.; Russell, J. T.; Saldaña, S. J.; Kumar, R.; Thackeray, M. M.; Curtiss, L. A.; Dravid, V. P.; Wolverton, C.; Hersam, M. C. Suppressing Manganese Dissolution from Lithium Manganese Oxide Spinel Cathodes with Single-Layer Graphene. *Adv. Energy Mater.* **2015**, *5*, 1500646−1500655.

(50) Aykol, M.; Kim, S.; Wolverton, C. Van Der Waals Interactions in Layered Lithium Cobalt Oxides. *J. Phys. Chem. C* **2015**, *119*, 19053−19058.

(51) Cho, J.-H.; Aykol, M.; Kim, S.; Ha, J.-H.; Wolverton, C.; Chung, K. Y.; Kim, K.-B.; Cho, B.-W. Controlling The Intercalation Chemistry to Design High-Performance Dual-Salt Hybrid Rechargeable Batteries. *J. Am. Chem. Soc.* **2014**, *136*, 16116−16119.

(52) Aykol, M.; Kirklin, S.; Wolverton, C. Thermodynamic Aspects of Cathode Coatings for Lithium-Ion Batteries. *Adv. Energy Mater.* **2014**, *4*, 1400690−1400700.

(53) Li, Q.; Liu, H.; Yao, Z.; Cheng, J.; Li, T.; Li, Y.; Wolverton, C.; Wu, J.; Dravid, V. P. Electrochemistry of Selenium with Sodium and Lithium: Kinetics and Reaction Mechanism. *ACS Nano* **2016**, *10*, 8788−8795.

(54) Bin, H.; Yao, Z.; Zhu, S.; Zhu, C.; Pan, H.; Chen, Z.; Wolverton, C.; Zhang, D. A High-Performance Anode Material Based on FeMnO3/graphene Composite. *J. Alloys Compd.* **2017**, *695*, 1223−1230.

(55) Wolverton, C. Prediction of Li Intercalation and Battery Voltages in Layered vs. Cubic LixCoO2. *J. Electrochem. Soc.* **1998**, *145*, 2424−2431.

(56) Wolverton, C.; Zunger, A. First-Principles Prediction of Vacancy Order-Disorder and Intercalation Battery Voltages in LixCoO2. *Phys. Rev. Lett.* **1998**, *81*, 606−609.

(57) Wolverton, C.; Zunger, A. Cation and Vacancy Ordering in LixCoO2. *Phys. Rev. B: Condens. Matter Mater. Phys.* **1998**, *57*, 2242−2252.

(58) Kresse, G.; Hafner, J. Ab Initio Molecular Dynamics for Liquid Metals. *Phys. Rev. B: Condens. Matter Mater. Phys.* **1993**, *47*, 558−561.

(59) Kresse, G.; Hafner, J. Ab Initio Molecular-Dynamics Simulation of the Liquid-Metal-Amorphous-Semiconductor Transition in Germanium. *Phys. Rev. B: Condens. Matter Mater. Phys.* **1994**, *49*, 14251−14269.

(60) Kresse, G.; Furthmüller, J. Efficiency of Ab-Initio Total Energy Calculations for Metals and Semiconductors Using a Plane-Wave Basis Set. *Comput. Mater. Sci.* **1996**, *6*, 15−50.

(61) Kresse, G. Efficient Iterative Schemes for Ab Initio Total-Energy Calculations Using a Plane-Wave Basis Set. *Phys. Rev. B: Condens. Matter Mater. Phys.* **1996**, *54*, 11169−11186.

(62) Blöchl, P. E. Projector Augmented-Wave Method. *Phys. Rev. B: Condens. Matter Mater. Phys.* **1994**, *50*, 17953−17979.

(63) Perdew, J. P.; Ernzerhof, M.; Burke, K. Rationale for Mixing Exact Exchange with Density Functional Approximations. *J. Chem. Phys.* **1996**, *105*, 9982−9985.

(64) Dudarev, S. L.; Savrasov, S. Y.; Humphreys, C. J.; Sutton, A. P. Electron-Energy-Loss Spectra and The Structural Stability of Nickel Oxide: An LSDA+U Study. *Phys. Rev. B: Condens. Matter Mater. Phys.* **1998**, *57*, 1505−1509.

(65) Chen, J.; Wu, X.; Selloni, A. Electronic Structure and Bonding Properties of Cobalt Oxide in the Spinel Structure. *Phys. Rev. B: Condens. Matter Mater. Phys.* **2011**, *83*, 245204−245210.

(66) Chen, J.; Selloni, A. Electronic States and Magnetic Structure at the Co3O4 (110) Surface: A First-Principles Study. *Phys. Rev. B: Condens. Matter Mater. Phys.* **2012**, *85*, 085306−085314.

(67) Wang, L.; Maxisch, T.; Ceder, G. Oxidation Energies of Transition Metal Oxides within the GGA+U Framework. *Phys. Rev. B: Condens. Matter Mater. Phys.* **2006**, *73*, 195107−195112.

(68) Saal, J. E.; Kirklin, S.; Aykol, M.; Meredig, B.; Wolverton, C. Materials Design and Discovery with High-Throughput Density Functional Theory: The Open Quantum Materials Database (OQMD). *JOM* **2013**, *65*, 1501−1509.

(69) Kirklin, S.; Saal, J. E.; Meredig, B.; Thompson, A.; Doak, J. W.; Aykol, M.; Rühl, S.; Wolverton, C. The Open Quantum Materials Database (OQMD): Assessing the Accuracy of DFT Formation Energies. *npj Comput. Mater.* **2015**, *1*, 15010−15024.

(70) Kirklin, S.; Saal, J. E.; Hegde, V. I.; Wolverton, C. High-Throughput Computational Search for Strengthening Precipitates in Alloys. *Acta Mater.* **2016**, *102*, 125−135.

(71) Zhou, F.; Marianetti, C. A.; Cococcioni, M.; Morgan, D.; Ceder, G. Phase Separation in LixFePO4 Induced by Correlation Effects. *Phys. Rev. B: Condens. Matter Mater. Phys.* **2004**, *69*, 201101−201104.

(72) Alberts, L.; Lee, E. W. Magnetostriction in Antiferromagnetic Nickel Oxide. *Proc. Phys. Soc., London* **1961**, *78*, 728−733.

(73) Akbarzadeh, A. R.; Ozoliņš, V.; Wolverton, C. First-Principles Determination of Multicomponent Hydride Phase Diagrams: Application to the Li-Mg-N-H System. *Adv. Mater.* **2007**, *19*, 3233−3239.

(74) Wolverton, C.; Yan, X.-Y.; Vijayaraghavan, R.; Ozoliņš, V. Incorporating First-Principles Energetics in Computational Thermodynamics Approaches. *Acta Mater.* **2002**, *50*, 2187−2197.

(75) Belsky, A.; Hellenbrandt, M.; Karen, V. L.; Luksch, P. New Developments in the Inorganic Crystal Structure Database (ICSD): Accessibility in Support of Materials Research and Design. *Acta Crystallogr., Sect. B: Struct. Sci.* **2002**, *58*, 364−369.

(76) Grindy, S.; Meredig, B.; Kirklin, S.; Saal, J. E.; Wolverton, C. Approaching Chemical Accuracy with Density Functional Calculations: Diatomic Energy Corrections. *Phys. Rev. B: Condens. Matter Mater. Phys.* **2013**, *87*, 075150−075157.

(77) Stevanović, V.; Lany, S.; Zhang, X.; Zunger, A. Correcting Density Functional Theory for Accurate Predictions of Compound Enthalpies of Formation: Fitted Elemental-Phase Reference Energies. *Phys. Rev. B: Condens. Matter Mater. Phys.* **2012**, *85*, 115104−115115.

(78) SGTE. *Thermodynamic Properties of Inorganic Materials*; Berlin, 1999.

(79) Nash, P. Thermodynamic Database. https://tptc.iit.edu/index.php/thermo-database.

(80) Li, Q.; Yao, Z.; Wu, J.; Mitra, S.; Hao, S.; Sahu, T. S.; Li, Y.; Wolverton, C.; Dravid, V. P. Intermediate Phases in Sodium Intercalation into MoS2 Nanosheets and Their Implications for Sodium-Ion Batteries. *Nano Energy* **2017**, *38*, 342−349.

(81) Liu, H.; Li, Q.; Yao, Z.; Li, L.; Li, Y.; Wolverton, C.; Hersam, M. C.; Dravid, V. P. Origin of Fracture-Resistance to Large Volume Change in Cu-Doped Co₃O₄ Electrode. *Adv. Mater.* **2017**, in press.

(82) He, K.; Yao, Z.; Hwang, S.; Li, N.; Sun, K.; Gan, H.; Du, Y.; Zhang, H.; Wolverton, C.; Su, D. Kinetically-Driven Phase Transformation during Lithiation in Copper Sulfide Nanoflakes. *Nano Lett.* **2017**, *17*, 5726−5733.

(83) Michel, K. J.; Ozoliņš, V. Native Defect Concentrations in NaAlH4 and Na3AlH6. *J. Phys. Chem. C* **2011**, *115*, 21443−21453.

(84) Michel, K. J.; Zhang, Y.; Wolverton, C. Fast Mass Transport Kinetics in B20H16: A High-Capacity Hydrogen Storage Material. *J. Phys. Chem. C* **2013**, *117*, 19295−19301.

(85) Michel, K. J.; Wolverton, C. Symmetry Building Monte Carlo-Based Crystal Structure Prediction. *Comput. Phys. Commun.* **2014**, *185*, 1389−1393.

(86) Ward, L.; Michel, K. *Materials/Mint: Initial Release*; 2016. doi.org/10.5281/zenodo.167890.

(87) Hart, G.; Forcade, R. Algorithm for Generating Derivative Structures. *Phys. Rev. B: Condens. Matter Mater. Phys.* **2008**, *77*, 224115−224126.

(88) Hart, G. L. W.; Forcade, R. W. Generating Derivative Structures from Multilattices: Algorithm and Application to Hcp Alloys. *Phys. Rev. B: Condens. Matter Mater. Phys.* **2009**, *80*, 014120−014127.

(89) Hart, G. L. W.; Nelson, L. J.; Forcade, R. W. Generating Derivative Structures at A Fixed Concentration. *Comput. Mater. Sci.* **2012**, *59*, 101−107.

(90) Cockayne, E.; van de Walle, A. Building Effective Models from Sparse but Precise Data: Application to an Alloy Cluster Expansion Model. *Phys. Rev. B: Condens. Matter Mater. Phys.* **2010**, *81*, 012104−012107.

(91) van de Walle, A. Multicomponent Multisublattice Alloys, Nonconfigurational Entropy and Other Additions to the Alloy

Theoretic Automated Toolkit. *CALPHAD: Comput. Coupling Phase Diagrams Thermochem.* **2009**, *33*, 266−290.

(92) van de Walle, A. Methods for First-Principles Alloy Thermodynamics. *JOM* **2013**, *65*, 1523−1532.

(93) Aydinol, M. K.; Kohan, A. F.; Ceder, G.; Cho, K.; Joannopoulos, J. Ab Initio Study of Lithium Intercalation in Metal Oxides and Metal Dichalcogenides. *Phys. Rev. B: Condens. Matter Mater. Phys.* **1997**, *56*, 1354−1365.

(94) van de Krol, R.; Goossens, A.; Meulenkamp, E. A. In Situ X-Ray Diffraction of Lithium Intercalation in Nanostructured and Thin Film Anatase TiO2. *J. Electrochem. Soc.* **1999**, *146*, 3150−3154.

(95) Li, Y.; Tan, B.; Wu, Y. Mesoporous Co3O4 Nanowire Arrays for Lithium Ion Batteries with High Capacity and Rate Capability. *Nano Lett.* **2008**, *8*, 265−270.

(96) Kim, H.; Seo, D.-H.; Kim, S.-W.; Kim, J.; Kang, K. Highly Reversible Co3O4/graphene Hybrid Anode for Lithium Rechargeable Batteries. *Carbon* **2011**, *49*, 326−332.

(97) Mai, Y. J.; Shi, S. J.; Zhang, D.; Lu, Y.; Gu, C. D.; Tu, J. P. NiO−graphene Hybrid as an Anode Material for Lithium Ion Batteries. *J. Power Sources* **2012**, *204*, 155−161.

(98) Sanville, E.; Kenny, S. D.; Smith, R.; Henkelman, G. Improved Grid-Based Algorithm for Bader Charge Allocation. *J. Comput. Chem.* **2007**, *28*, 899−908.

(99) Tang, W.; Sanville, E.; Henkelman, G. A Grid-Based Bader Analysis Algorithm without Lattice Bias. *J. Phys.: Condens. Matter* **2009**, *21*, 084204−084210.

(100) Chae, B.-M.; Oh, E.-S.; Lee, Y.-K. Conversion Mechanisms of Cobalt Oxide Anode for Li-Ion Battery: In Situ X-Ray Absorption Fine Structure Studies. *J. Power Sources* **2015**, *274*, 748−754.

(101) Li, Q.; Wu, J.; Yao, Z.; Thackeray, M. M.; Wolverton, C.; Dravid, V. P. Dynamic Imaging of Metastable Reaction Pathways in Lithiated Metal Oxide Electrodes; Submitted.

(102) Evmenenko, G.; Fister, T. T.; Buchholz, D. B.; Li, Q.; Chen, K.-S.; Wu, J.; Dravid, V. P.; Hersam, M. C.; Fenter, P.; Bedzyk, M. J. Morphological Evolution of Multilayer Ni/NiO Thin Film Electrodes during Lithiation. *ACS Appl. Mater. Interfaces* **2016**, *8*, 19979−19986.

(103) Zhuravlev, Y. N.; Obolonskaya, O. S. Structure, Mechanical Stability, and Chemical Bond in Alkali Metal Oxides. *J. Struct. Chem.* **2010**, *51*, 1005−1013.

(104) Häglund, J.; Fernández Guillermet, A.; Grimvall, G.; Körling, M. Theory of Bonding in Transition-Metal Carbides and Nitrides. *Phys. Rev. B: Condens. Matter Mater. Phys.* **1993**, *48*, 11685−11691.